Journal of Power Sources 449 (2020) 227574

Contents lists available at ScienceDirect

Journal of Power Sources

journal homepage: www.elsevier.com/locate/jpowsour

Selective doping to relax glassified grain boundaries substantially enhances the ionic conductivity of $LiTi_2(PO_4)_3$ glass-ceramic electrolytes

Shanshan Duan [a,1], Junxi Yu [b,c,1], Yuanwei Sun [d], Aolin Li [c], Shulin Chen [d], Ke Qu [b,d], Zhengping Ding [d], Zixian Liu [a], Yuhang Li [a], Can Huang [a], Min Liu [e], Jiale Liu [a], Jianpeng Shi [e], Boyuan Huang [b], Xiaocong Tian [a], Shuen Hou [a], Shuhong Xie [c], Yunya Liu [c], Peng Gao [d], Jiangyu Li [b,f,*], Hongyun Jin [a,**]

[a] Engineering Research Center of Nano-Geomaterials of Ministry of Education, Faculty of Materials Science and Chemistry, China University of Geosciences, Wuhan, 430074, China
[b] Shenzhen Key Laboratory of Nanobiomechanics, Shenzhen Institutes of Advanced Technology, Chinese Academy of Sciences, Shenzhen, 518055, China
[c] Key Laboratory of Low Dimensional Materials and Application Technology of Ministry of Education, School of Materials Science and Engineering, Xiangtan University, Xiangtan, 411105, China
[d] International Center for Quantum Materials and Electron Microscopy Laboratory, School of Physics, Peking University, Beijing, 100871, China
[e] Department of Technology Centre of Dongfeng Motor Group Co. LTD, Wuhan, 430058, China
[f] Dept. of Mechanical Engineering, University of Washington, WA, 98195, USA

HIGHLIGHTS

- Glassified boundary lead to high ionic conductivity in glass-ceramic electrolytes.
- The relaxed glassified boundary can be induced by boron.
- Electrochemical strain microscopy can probe local ionic activity at the nanoscale.

GRAPHICAL ABSTRACT

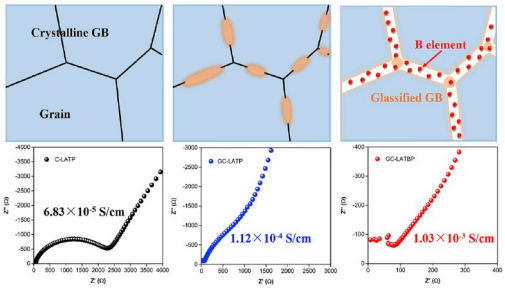

ARTICLE INFO

Keywords:
Glass-ceramic electrolytes
Grain boundary structure
Selective doping
Electrochemical strain microscopy

ABSTRACT

Glass-ceramic electrolytes are promising for all-solid-state batteries, yet their enhanced ionic conductivity is not well understood. We investigate structural difference between ceramic and glass-ceramic $Li_{1.3}Al_{0.3}Ti_{1.7}(PO_4)_3$ tuned by boron, which is found to enhance conductivities of glass-ceramics by one order of magnitude, yet reduces that of ceramics. Raman and Magic Angle Spinning Nuclear Magnetic Resonance spectra indicate boron are primarily contained in glass phase, while electron energy-loss spectroscopy and high-resolution transmission electron microscopy reveal inhomogeneous distribution of boron and glassified grain boundaries. This substantially reduces interfacial resistance at grain boundaries with little effect on bulk resistance, which is further

* Corresponding author. Shenzhen Key Laboratory of Nanobiomechanics, Shenzhen Institutes of Advanced Technology, Chinese Academy of Sciences, Shenzhen, 518055, China.
** Corresponding author.
E-mail addresses: jjli@uw.edu (J. Li), jinhongyun@cug.edu.cn (H. Jin).
[1] These authors contributed equally to this work.

https://doi.org/10.1016/j.jpowsour.2019.227574
Received 7 October 2019; Received in revised form 28 November 2019; Accepted 5 December 2019
Available online 11 December 2019
0378-7753/

supported by spatial and spectroscopic electrochemical strain microscopy. The grain boundary resistance of ceramics, on the other hand, is increased by boron. We thus establish that lower interfacial resistance at glassified grain boundaries is responsible for higher conductivity in glass-ceramics, while boron can relax their grain boundaries even further.

1. Introduction

With ever-growing demand for high-performance, safe and environmentally friendly lithium-ion batteries (LIBs), increasing attentions have been devoted to all-solid-state batteries that utilize solid electrolytes, which have many advantages over conventional LIBs [1–3], including higher current densities and faster charging/discharging rates [4], better safety [5], and enhanced energy density [6]. Despite such promises, the development of all-solid-state batteries has been largely hindered by the lack of solid electrolytes with sufficient high ionic conductivity [7], and hybrid glass-ceramic electrolytes such as Li_2O–Al_2O_3–TiO_2–P_2O_5 with ionic conductivity approaching 10^{-3} S cm^{-1} at room temperature have emerged as an attractive alternative [8,9]. Most of the previous studies on glass-ceramic electrolytes focused on optimizing their crystalline microstructure to further improve their overall conductivity [10,11]. For example, it has been suggested that aliovalent substitution can change the size of the lithium ion transport network in crystalline phase, resulting in conductivity of 3.85×10^{-4} S cm^{-1} that is 2–3 times higher than undoped $Li_{1.4}Al_{0.4}Ge_{1.6}(PO_4)_3$ glass-ceramic [12]. Furthermore, increased conductivity of 7.25×10^{-4} S cm^{-1} can also be achieved in $Li_{1.5}Al_{0.5}Ge_{1.5}(PO_4)_3$ glass-ceramic with well-developed crystalline phase and dense microstructure, achieved by the addition of low melting oxides such as B_2O_3 [13]and Li_2O [14] to accelerate the crystallization process. The glass phase in glass-ceramic electrolytes, on the other hand, has received less attention.

While optimizing the crystalline phase of the glass-ceramic electrolytes has been effective in enhancing the ionic conductivity, it is important to note that glass electrolytes actually possess much lower ionic conductivity compared to their crystalline counterparts, and thus it is quite counterintuitive that ionic conductivity of hybrid glass-ceramic electrolytes is higher than pure ceramic phases [15,16]. For example, the ionic conductivity of $Li_{1.3}Al_{0.3}Ti_{1.7}(PO_4)_3$ glass-ceramic is about 1×10^{-4} S cm^{-1}, much higher than 6×10^{-5} S cm^{-1} of $Li_{1.3}Al_{0.3}Ti_{1.7}(PO_4)_3$ ceramic [17,18], while the corresponding conductivity of glass phase is orders of magnitude smaller, in the range of 10^{-10}–10^{-8} S cm^{-1} [19–21]. This begs for an explanation, and the reason may lie in grain boundaries of ceramics, which exhibit high resistance to the ionic conduction [22]. Indeed, it has been observed that structural and chemical deviations of several unit cells thick exist at the grain boundaries, which blocks the ionic conduction in ceramic electrolytes [23]. Whereas for glass-ceramics, such high resistive grain boundaries might have been relaxed by amorphous interface [15,24] that exhibits unusual semi-crystalline and semi-glassy structure at the atomic scale, leading to lower interfacial resistance and thus higher overall ionic conductivity [16,25]. Such hypothesis, however, has neither been firmly established nor further explored.

In order to understand the mechanism responsible for the enhanced ionic conductivity in glass-ceramic electrolytes, we investigate the structural difference between the ceramic and glass-ceramic and its correlation with their ionic conduction, using $Li_{1.3}Al_{0.3}Ti_{1.7}(PO_4)_3$ (LATP) as the model system. Considering boron as a common glass network former that has been used to improve the conductivity of glass electrolyte [26,27], we seek to tune the glass phase in LATP glass-ceramic by boron, which simultaneously serves as a tracer in the glass phase for us to assess its effect on the microstructure. Quite interestingly, it is found that boron doping enhances the ionic conductivities of both glass and glass-ceramic, yet reduces the ionic conductivity of pure ceramics. Further studies by Raman spectra and Magic Angle Spinning (MAS) Nuclear Magnetic Resonance (NMR) spectra indicate that boron elements are primarily contained in the glassy phase of glass-ceramic, while electron energy-loss spectroscopy (EELS) in combination with high-resolution transmission electron microscopy (HR-TEM) suggest that the distribution of B is inhomogeneous, which could result in classification and relaxation of grain boundaries. This has profound influence on the ionic conduction of glass-ceramics. Indeed, it is found from electrochemical impedance spectroscopy (EIS) that boron substantially reduces interfacial resistance at the grain boundaries, while it have little effect on the bulk resistance, which is further supported by the localized electrochemical strain microscopy (ESM) studies at the nanoscale. Combing all these observation together, we establish that lower interfacial resistance at glassified grain boundaries is responsible for the higher ionic conductivity in glass-ceramic electrolytes, while boron doping can relax the grain boundary resistance even further. The work thus sheds considerable insight into the conduction mechanism in glass-ceramics, and offers an effective strategy for improving their ionic conductivity further.

2. Results and discussion

Glass-ceramic samples of $Li_{1.3}Al_{0.3}Ti_{1.7}(PO_4)_3$ (GC-LATP) and $Li_{1.3}Al_{0.2}B_{0.1}Ti_{1.7}(PO_4)_3$ (GC-LATBP) were prepared using conventional melt-quenching method [28]. For comparison, glass of LATP (G-LATP) and LATBP (G-LATBP) were processed by skipping the post-heat treatment of glass-ceramics. The corresponding ceramics (C-LATP and C-LATBP) were obtained through conventional solid state method [29]. The powder XRD patterns of both ceramic and glass-ceramic samples are shown in Fig. 1a, wherein the main phase corresponds to $LiTi_2(PO_4)_3$ crystallite (JCPDS NO.35–0754), while $AlPO_4$, the most common secondary phase [30], which is also observed in both glass-ceramic samples. By comparing the maximum peak intensities of $LiTi_2(PO_4)_3$ and $AlPO_4$, the concentration of $AlPO_4$ is found to be almost identical in GC-LATBP and GC-LATP, estimated to be 14% and 15%, respectively. Furthermore, the crystallinity is calculated to be 95% and 89% for GC-LATP and GC-LATBP (Fig. 1b), as detailed in the Supporting Information (SI), while that of C-LATP and C-LATBP is estimated to be 100% and 93%, respectively. Not surprisingly, the crystallinity decreases after boron doping for both ceramic and glass-ceramic, since its incorporation promotes the glass-forming tendency [31]. Importantly, the crystallinity of both glass-ceramic samples are pretty high, and the volume fraction of glass phase is only about 10% or less. Additional XRD patterns of glass samples are shown in Fig. S1, both of which exhibit weak and broad peaks characteristic of the amorphous phase. Furthermore, the microstructural morphology of glass-ceramics before and after boron doping is found to be almost identical, as seen from cross-section SEM images (Fig. S2 and Fig. S3) as well as the corresponding EDS elemental mappings. No significant difference is observed between microstructures of C-LATP and C-LATBP as well (Fig. S4). Finally, the densities of GC-LATP, GC-LATBP, C-LATP and C-LATBP are measured to be 2.57 g cm^{-3}, 2.59 g cm^{-3}, 2.49 g cm^{-3}, 2.54 g cm^{-3}, respectively. Thus the relative densities calculated with a theoretical density of 2.94 g cm^{-3} [18] are quite similar, measured to be 87.5%, 88.3%, 84.7%, 86.3%, respectively. All these data thus suggest that only minor differences exist in microstructural morphology, crystallinity, and porosity among GC-LATP, GC-LATBP, C-LATP and C-LATBP, yet their ionic conductivities are found to be substantially different.

We then evaluate total ionic conductivity with an equivalent circuit model for each sample using electrochemical impedance spectroscopy (EIS), and the complex impedance spectrum of glass-ceramics, glasses,

and ceramics measured at room temperature are shown in Fig. 2a, c, d. It is observed that both spectra consist of semicircle at high frequency due to bulk, grain boundary, interfacial resistance and a spike in the low-frequency region due to the double-layer impedance at the contact between the sample and metal electrodes [8]. Immediately, it is observed that while glass-ceramics have slightly lower crystallinity and similar density compared to their ceramic counterparts, their ionic conductivities are substantially higher, suggesting that the glass phase, even with small volume fraction around 10% or less, can enhance the ionic conductivity of glass-ceramics. More importantly, it is found that after boron doping, the ionic conductivity of glass-ceramic increases by one order of magnitude, jumping from 1.12×10^{-4} S cm^{-1} to 1.03×10^{-3} S cm^{-1}, whereas the corresponding active energy (E_a) decreases from 0.27 eV to 0.17 eV (Fig. 2b). Similar enhancement is also observed in pure glass, whose conductivity increases from 8.58×10^{-9} S cm^{-1} to 6.01×10^{-8} S cm^{-1} after boron doping (Fig. 2c). Opposite trend, however, is observed in pure ceramics, wherein ionic conductivity decreases from 6.83×10^{-5} S cm^{-1} to 3.23×10^{-5} S cm^{-1} after boron doping (Fig. 2d). This further demonstrates that the glass phase in the glass-ceramic is critical, despite its small volume fraction.

In order to understand the opposite effect of boron in ceramic and glass-ceramic, and more importantly, to figure out the microscopic mechanisms responsible for the higher conductivity in glass-ceramics, we examine the fine structural changes after boron doping not reflected in their crystallinity and density. Magic angle spinning-nuclear magnetic resonance (MAS-NMR) has been used for decades to study the chemical structure and order of materials, revealing the structural units not only in glasses but also in the corresponding crystallites. In our study, ^{11}B MAS-NMR spectra of C-LATBP, G-LATBP and GC-LATBP samples were recorded at 298 K as presented in Fig. 3a, b, c. All three samples exhibit different chemical shift of BO_4 between −10 and 2 ppm and BO_3 between 10 and 15 ppm [31]. In particular, it is observed that broad resonances are centered at 12.806 ppm (BO_3) and −2.278 ppm (BO_4) for C-LATBP, while for G-LATBP they shift to 7.811 ppm and −4.751 ppm, respectively, reflecting changes in B coordination mode and the surrounding environment. For GC-LATBP, the resonances shift to 8.609 ppm and −5.015 ppm, respectively, much closer to those of pure glass. Furthermore, the resonant peaks of GC-LATBP can be fitted by linear combination of G-LATBP and C-LATBP using Mestrenova software, as shown in Fig. 3c. The integrated intensity of glass and ceramic phases are found to be 75% and 25% respectively, indicating that B is primarily contained in the glass phase.

In order to understand the structural change in glass phase after boron doping, Raman spectra of ceramic, glass, and glass-ceramic samples were measured in the range of 400–1200 cm^{-1}, as shown in Fig. 3d, e, f. We focus on peaks corresponding to TiO_4 and TiO_6 units in the range between 500 and 900 cm^{-1}, which signify a glass phase that is not found in the pure ceramics [32,33], as confirmed by our data in Fig. 3d. It is found that TiO_4 unit near 750 cm^{-1} [34,35] decreases and TiO_6 unit near 600 cm^{-1} [33] increases for glass-ceramic sample, and similar trend is also observed in pure glass, suggesting that after B doping, part of TiO_4 transforms into TiO_6. Considering titanium as a common glass network intermediate and boron as a common glass network former, this suggests that the introduction of B disrupts the original glass network such that some TiO_4 groups no longer act as network former but transform to TiO_6 units. Moreover, the increased ^{31}P MAS-NMR peak width in GC-LATBP (Fig. S5) suggests a modified environment for P as well and likely distortion of P–O bonds, which could arise from formation of new chemical bonds after boron doping.

The high-resolution transmission electron microscopy (HR-TEM) is then adopted to examine the atomic structure of C-LATP, GC-LATP and GC-LATBP, as shown in Fig. 4a–c. It can be seen from Fig. 4a that the grain boundaries of C-LATP are composed of atom columns with certain degree of order, which are similar to the previous report [23]. Whereas for GC-LATP in Fig. 4b, amorphous phase about 2 nm thick is also found at the grain boundary in addition to the ordered atom column. Interestingly, strip-like glassfield grain boundaries about 3–4 nm thick are observed in GC-LATBP, as shown in Fig. 4c, suggesting that the grain boundaries are further glassified after B doping, which reduces the overall crystallinity of glass-ceramic slightly. Additional HR-TEM images supporting this observation are presented in Figs. S6 and S7. Furthermore, high angle annular dark field (HAADF) image of GC-LATBP is shown Fig. 4d, and the electron energy-loss spectroscopy (EELS) between 100 and 350 eV in Fig. 4e shows peak of B K-edge at ~188 eV. The corresponding EELS intensity map formed by the B K-edge of GC-LATBP sample in Fig. 4f suggests that B is inhomogeneously distributed and aggregate into strips, similar to the glassified grain boundaries in Fig. 4c. This observation is further supported by the scanning transmission electron microscopy (STEM) images and corresponding element mappings of GC-LATBP sample in Fig. S8, showing that all the elements except B are homogeneously distributed without apparent aggregation. We thus conclude that the inhomogeneously

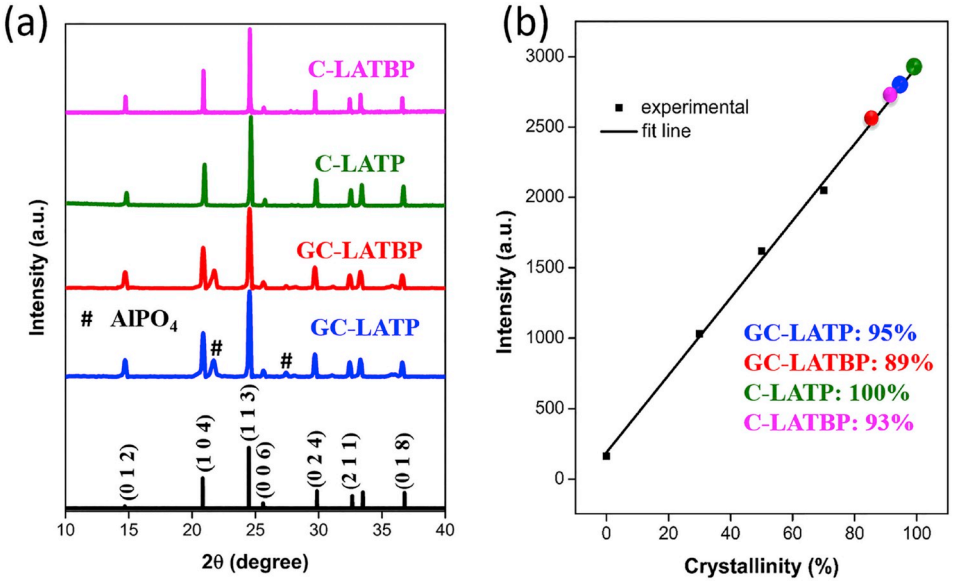

Fig. 1. Crystallinity of GC-LATP, GC-LATBP, C-LATP and C-LATBP samples; (a) X-ray diffraction patterns; (b) standard curves of crystallinity based on experimental measurement and fitting.

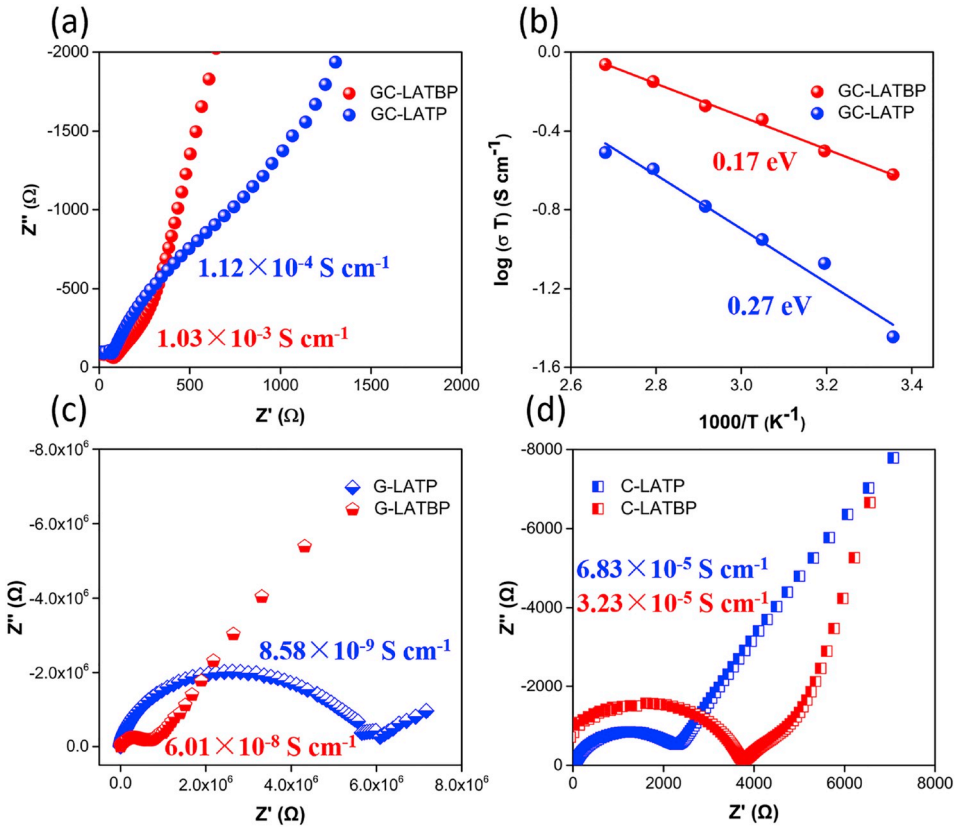

Fig. 2. Complex impedance plots measured at room temperature for (a) GC-LATBP and GC-LATP, (c) G-LATBP and G-LATP, and (d) C-LATBP and C-LATP; (b) Arrhenius plots of conductivity for GC-LATBP and GC-LATP.

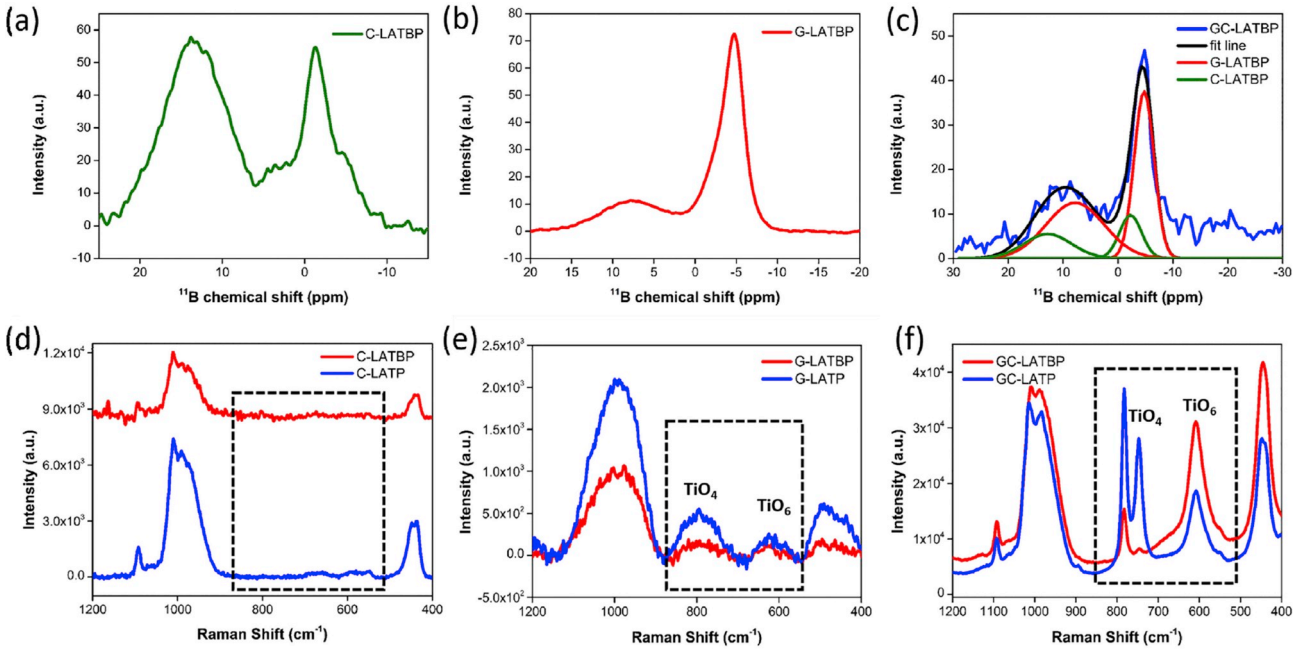

Fig. 3. ^{11}B MAS-NMR spectra of (a) C-LATBP, (b) G-LATBP and (c) GC-LATBP samples. Raman spectra in the range of 400–1200 cm^{-1} recorded for the (d) C-LATBP and C-LATP, (e) G-LATBP and G-LATP, and (f) GC-LATBP and GC-LATP.

distributed B could largely aggregate at grain boundaries, generating glassified relaxed boundary structure.

In order to investigate whether the glassified grain boundaries would affect the ionic conduction, we resolve the total ionic conductivity measured by EIS into contributions from bulk and grain boundaries using an equivalent circuit model, as schematically shown in Fig. S9, consisting of a constant phase elements (CPE_1) connected in parallel with a resistor (R_1) representing bulk grains, a CPE_2 in parallel with R_2

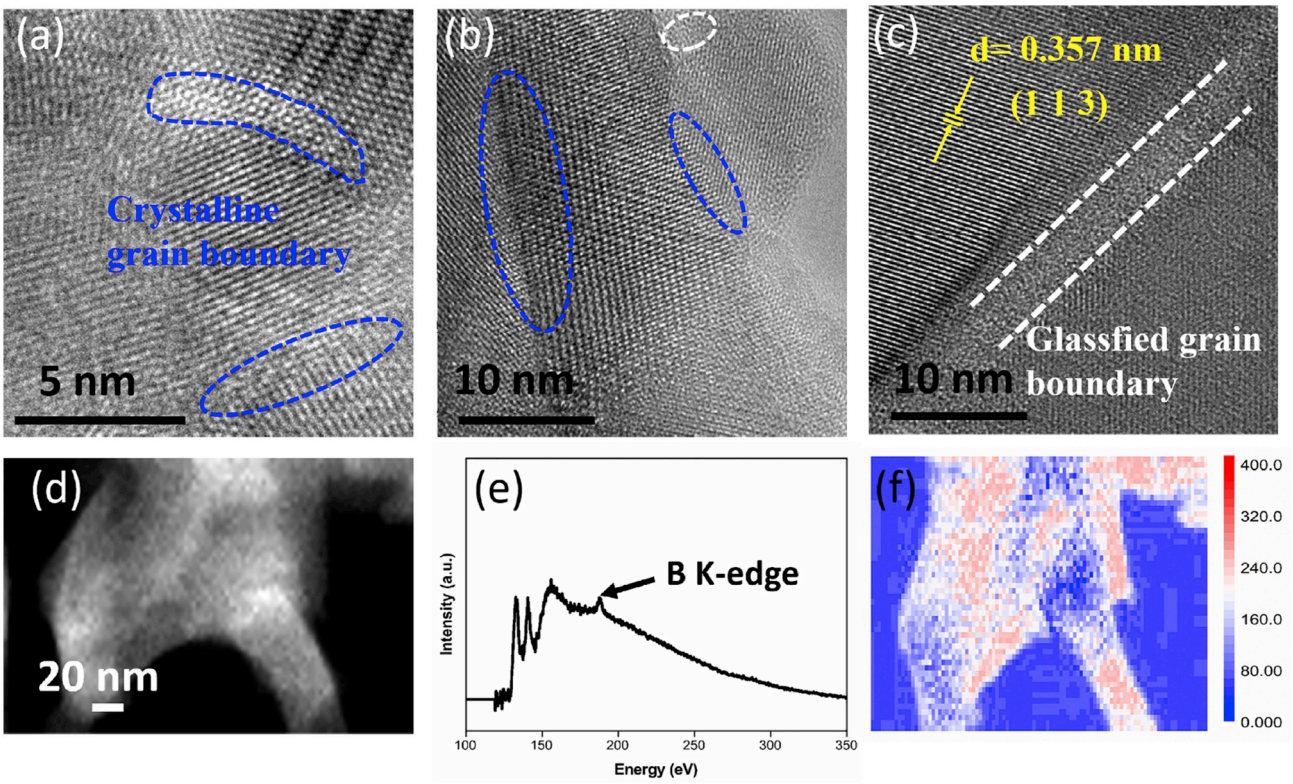

Fig. 4. HRTEM images of (a) C-LATP sample, (b) GC-LATP and (c) GC-LATBP sample; (d) HAADF image and (e) corresponding EELS with energy 100–350 eV showing peak of B K-edge; (f) EELS intensity map formed by the B K-edge.

representing grain boundaries, and a CPE_3 in parallel with R_3 along with a Warburg impedance (W) representing the electrode phenomena. The impedance data are summarized in Table S1, and the apparent bulk and grain boundary conductives are summarized in Table 1. Indeed, we notice that boron doping does not affect bulk conductivity of glass-ceramic much, while it substantially increases grain boundary conductivity by one order of magnitude, resulting in one order of magnitude enhancement in its overall conductivity. This can also be verified by the similar bulk activation energy between GC-LATP (0.16 eV)and GC-LATBP (0.13 eV) (Fig. S10). When boron is doped into pure ceramics, on the other hand, the conductivities of both bulk and grain boundary decrease significantly, which could due to the formation of second amorphous phase. We thus conclude that the glassified grain boundary is the main reason for the enhanced ionic conductivity of glass-ceramic, while boron doping helps relax grain boundary resistance even further.

Sequential excitation electrochemical strain microscopy (SE-ESM) excites the sample using a sequence of AC voltages with predefined amplitude and a range of frequencies across contact-resonance frequencies of each pixel in an image, wherein the excitation voltage is concentrated on only one frequency at a time without resonance frequency tracking [36,37]. We adopted SE-ESM to probe local ionic conductivity of both GC-LATBP and GC-LATP at the nanoscale, wherein 3 V AC voltages with a sequence of excitation frequencies were applied one by one through a conductive tip, inducing local ionic fluctuation and thus mechanical vibration due to electrochemical strain [38]. The mappings of ESM amplitude at each frequency is shown in Figs. S11 and S12, while intrinsic ESM amplitude reconstructed from simple harmonic oscillator model [39] are shown in Fig. 5a and b, wherein the high fidelity of fitting is evident from the mappings of R^2 coefficient in Fig. S13. Much higher ESM response is observed in LATBP, consistent with macroscopic measurement, which can also be seen from the comparision of histogram distributions (Fig. 5c). The ESM response of GC-LATBP is 3.90 p.m. ± 0.64 p.m., while that of GC-LATP is 2.60 p.m. ± 0.35 p.m., suggesting higher local ionic conductivity of the former [40]. Note that GC-LATBP exhibits much stronger nonuniformity, consistent with the inhomogeneous distributution of B. Furthermore, the mappings and histogram distributions of quality factor are shown in Fig. 5d, e, f, which is inversely proportional to energy dissipation associated with redistribution of lithium ions and thus reflects the energy barrier. It is observed that the quality factor of GC-LATBP is 28.32 ± 5.20, while that of GC-LATP is 23.27 ± 3.69, indicating that GC-LATBP has lower dissipation and energy barrier compared to GC-LATP, consistent with their respective activation energy in Fig. 2b.

The comparision of local ionic conductivities of GC-LATBP and GC-LATP can be better visualized from the point-wise relaxation dynamics [40] after removal of a negative DC bias of 10 V, as shown in Fig. 6. The ESM response versus excitation frequency is first examined, and classified into high and low response regions depending on its amplitudes, with representative cuves shown in Fig. 6a and b. It is clear that for both cases, GC-LATBP has higher amplitude than GC-LATP. Relaxation curves for high and low response regions are then measured as shown in Fig. 6c and d, revealing local dynamics of bias induced motion of lithium ions. The application of negative DC increases the concentration of lithium ions under the probe [40] and thus the ESM response, and after the removal of DC, the response relaxes back to the ground state, wherein faster relaxation is evident in GC-LATBP. The realxation curves are fitted by exponential function $A(0,t) = Aexp\left(-t/\tau\right) + A_0$, from which the

Table 1
Conductivities of bulk and grain boundary for GC-LABTP, GC-LATP, C-LATBP and C-LATP samples.

Sample	bulk conductivity (S cm^{-1})	Grain boundary conductivity (S cm^{-1})
GC-LATP	2.02×10^{-3}	1.22×10^{-4}
GC-LATBP	3.04×10^{-3}	1.52×10^{-3}
C-LATP	2.55×10^{-3}	6.96×10^{-5}
C-LATBP	1.41×10^{-3}	3.48×10^{-5}

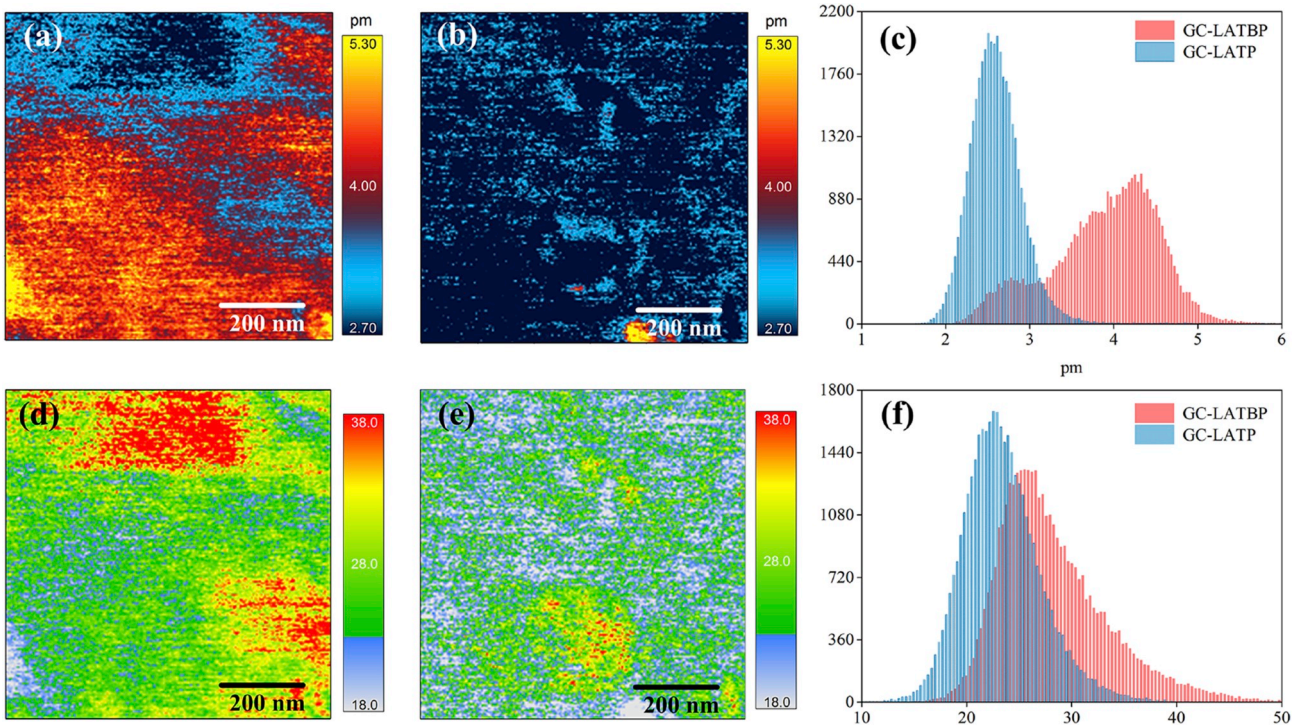

Fig. 5. Mappings of SE-ESM amplitude of (a) GC-LATBP and (b) GC-LATP, and (c) the corresponding histogram distribution; mappings of SE-ESM quality factor of (d) GC-LATBP and (e) GC-LATP, and (f) the corresponding histogram distribution.

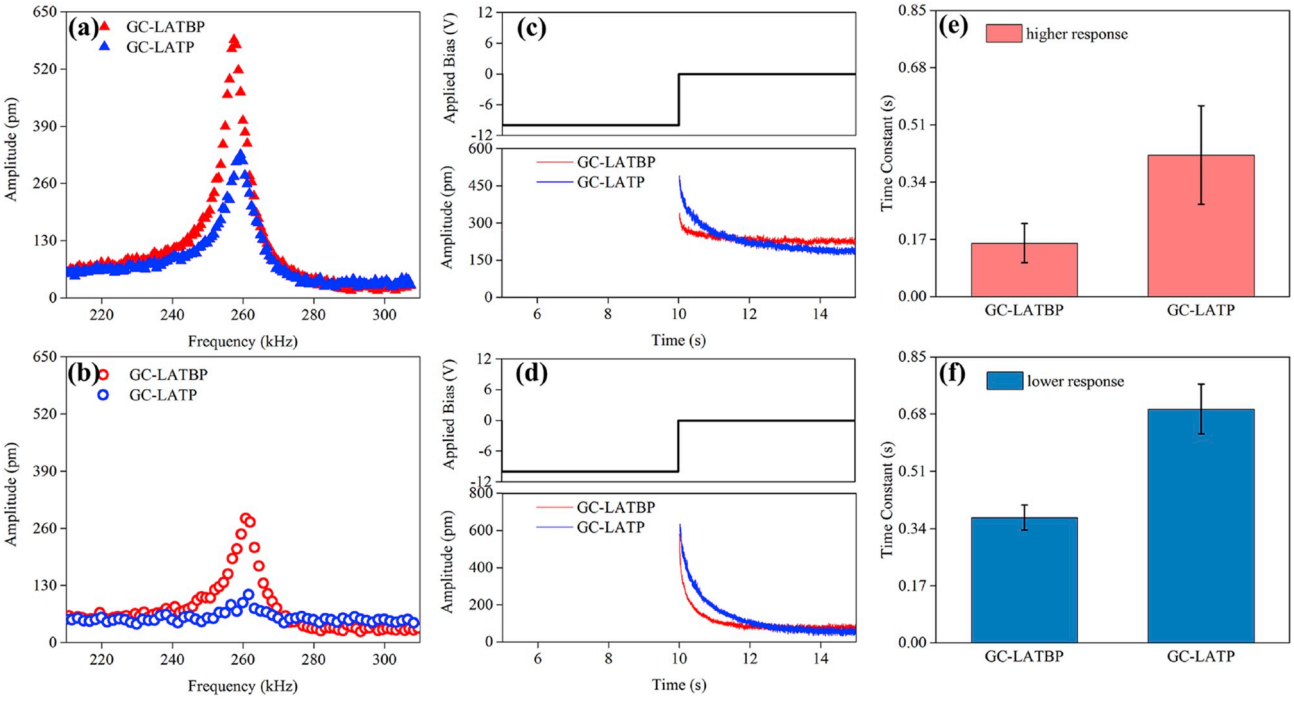

Fig. 6. Relaxation dynamics of local electrochemical strain in GC-LATBP and GC-LATP at room temperature. ESM response versus excitation frequency for (a) high and (b) low response regions. ESM signal as a function of time after removal of negative voltage pulse for (c) high and (d) low response regions. Comparison of time constants of (e) high and (f) low response regions, averaged over 7 points in each area.

time constants can be determined and compared, as presented in Fig. 6e and f. It is observed that the time constant of LABTP is much smaller than that of LATP in both high and low response region, confirming its much higher local diffusivity [41].

We highlight the key insight uncovered in this study, that the glassified grain boundaries is responsible for enhanced ionic conductivities in glass-ceramics. While the idea has been put forward before, we use boron as a tracer in glass-ceramics as well as glass and ceramics, in combination with systematic structural and functional characterizations, including XRD, NMR, Raman, HRTEM, EIS, and ESM, to establish

a strong experimental footing for the proposal. This has not been reported before to our best knowledge, and the concept can be utilized to improve the ionic conductivity of electrolytes for solid state batteries.

3. Conclusions

In summary, C-LATP, C-LATBP, G-LATP, G-LATBP, GC-LATP and GC-LATBP were synthesized, and it is found that boron primarily fills in the amorphous network and further relaxes the glassified grain boundaries, resulting in total ionic conductivity up to 10^{-3} S cm^{-1} that is one order of magnitude higher than GC-LATP in the absence of boron. This work thus clarifies the mechanism responsible for enhanced ionic conductivity in glass-ceramics, and provides an effective strategy to optimize the glass-ceramic electrolytes further.

4. Experimental section

Materials synthesis: Glass-ceramics of $Li_{1.3}Al_{0.3}Ti_{1.7}(PO_4)_3$ (GC-LATP) and $Li_{1.3}Al_{0.2}B_{0.1}Ti_{1.7}(PO_4)_3$ (GC-LATBP) were prepared using conventional melt-quenching method [28]. Stoichiometric amounts of lithium carbonate Li_2CO_3 (AR, ≥99.9%), aluminium oxide Al_2O_3 (AR, ≥99.9%), boric acid H_3BO_3 (AR, ≥99.5%), titanium oxide TiO_2 (AR, ≥99.9%) and ammonium dihydrogen phosphate $NH_4H_2PO_4$ (AR, ≥99.9%) were homogeneously mixed through wet ball-milling, and the raw materials were put into electrically heated furnace for melting. The furnace was firstly set to 700 °C for 1 h, allowing for the decomposition of the raw materials, and then raised to 1500 °C and held there for 2 h before quenching in water. The quenched glass was pulverized to obtain glass powders by ball-milling using a planetary ball mill for 6 h. The glass powder was put into a cylindrical pressing mold (10 mm in diameter) and pressed under a uniaxial pressure of 200 MPa. The pressed pellets were crystallized at 950 °C for 2 h and slowly cooled down to room temperature at the rate of 5 °C min^{-1} to obtain the glass-ceramic.

For comparison, glass of LATP (G-LATP) and LATBP (G-LATBP) were also processed by skipping the 950 °C post-heat treatment of glass-ceramics. The corresponding ceramics (C-LATP and C-LATBP) were obtained through conventional solid state method [29]. The same stoichiometric raw materials were homogeneously mixed through wet ball-milling and then annealed at 700 °C for 4 h. Subsequently, the precursor powders were pressed under a pressure of 200 MPa and then heated at 950 °C for 2 h.

Characterization: The powder X-ray diffraction (XRD) patterns were recorded with a D8-FOCUS X-ray diffractometer using $CuK_{\alpha 1}$ radiation ($\lambda = 0.15405$ nm) after the pellets were ground to fine powder with an agate mortar and pestle. HR-TEM images and EDS mapping were carried out using Tecnai F20 at 200 kV with an Oneview IS (Gatan) camera and Oxford X-max^N TSR EDS detector. The EELS and STEM were acquired by Nion Ultra STEM™ 200 microscope operating at 60 kV. The probe convergence semi-angle was 35 mrad and the collection semi-angle was 24.9 mrad. The morphology images and element distribution of the cross-section were acquired using a SU8010 field scanning electron microscope (SEM) and energy dispersive X-ray spectroscopy (EDS). Prior to image acquisition the cross-section of the pellets were sputtered with gold. The stoichiometry of the sintered samples was analyzed by X-ray fluorescence spectroscopy (XRF). A typical result is shown in Table S2, which suggested loss of lithium content resulting from the high temperature involved in the fabrication process.

Raman spectra were recorded in the range of 100–1500 cm^{-1} using a RM-1000 Raman spectroscopy with a 532 nm laser. Magic Angle Spinning (MAS) Nuclear Magnetic Resonance (NMR) spectra were recorded on an Agilent 600 DD2 spectrometer at a resonance frequency of 242.76 MHz and 192.39 MHz for ^{31}P and ^{11}B, respectively. Samples were placed in the magnet with a 4 mm MAS probe operating at 15 kHz spinning speed.

Both GC-LATP and GC-LATBP samples were polished and attached on a conductive tape for electrochemical strain microscopy (ESM) [41–44] measurement using an Asylum Research Cypher ES atomic force microscope (AFM) under nitrogen flow at room temperature with electric ASYELEC-01 probe having spring constant of 2 N m^{-1} and resonance frequency in air around 70 kHz. Mappings of ESM response were obtained with 2 V AC voltage using dual amplitude resonance tracking technique (DART) [45] and fitted by simple harmonic oscillator model (SHO) [39]. Point-wise relaxation measurement was carried out after −10 V applied to the tip over 5 s to monitor the evolution of ESM response versus time, enabling characterization of local diffusivity.

Before impedance ($Z^* = Z' - iZ''$) measurements for ionic conductivity using Zennium X electrochemical workstation in the frequency range from 1 Hz to 10 MHz, both sides of the samples were polished to a smooth surface, the thickness varied in range of 0.98 mm–1.04 mm. Au was sputtered onto the surface of the electrolytes as blocking electrodes. THALES software was used for data acquisition and processing, and the conductivity can be calculated from $\sigma = d/SR$, where d is the sample thickness, S is the area of the electrolyte and R is resistance of the corresponding resistance. When calculated total conductivities, R is the sum of R_1 and R_2. The conductivity of samples was measured at different temperatures from 25 °C to 120 °C on a controlled electric hot plate, and the activation energy is calculated from the Arrhenius equation [2]: $\sigma = \sigma_0 exp\left(-E_a/k_B T\right)$.

Author contributions

L. J. Y. and J. H. Y. conceived and supervised the project. D. S. S. carried out the experiments. Y. J. X. performed the ESM measurements. S. Y. W. performed the TEM measurements. L. Z. X, L. Y. H., H. C., L. M. and L. J. L assisted D. S. S. in making some materials characterizations. L. A. L. and H. B. Y. assisted Y. J. X. in analyzing ESM data. C. S. L., Q. K. and D. Z. P. assisted in analyzing TEM data. G. P., L. Y. Y., X. S. H., H. S. E., T. X. C. and S. J. P. assisted during manuscript preparation. D. S. S. and Y. J. X. contributed equally to this work.

Declaration of competing interest

The authors declare that they have no known competing financial interests or personal relationships that could have appeared to influence the work reported in this paper.

Acknowledgments

This work is supported in part by National Natural Science Foundation of China (11627801), National Key Research Program of China (2016YFA0201001), Shenzhen Science and Technology Innovation Committee (KQTD20170810160424889, JCYJ20170818155813437), the Instrument Developing Project of Chinese Academy of Sciences (No. ZDKYYQ20180004), Major scientific and technological innovation in Hubei (2017AAA112 and 2018AAA015), Opening Project of Engineering Research Center of Nano-Geo Materials of Ministry of Education of China University of Geosciences (NGM2018KF021), Laboratory Open Foundation of 2017-2018 Academic Year (SKJ2018070 and SKJ2018065). P. G. also acknowledges the support from the National Natural Science Foundation of China (51672007). We gratefully acknowledge Electron Microscopy Laboratory in Peking University for the use of electron microscope.

Appendix A. Supplementary data

Supplementary data to this article can be found online at https://doi.org/10.1016/j.jpowsour.2019.227574.

References

[1] C. Luo, X. Ji, J. Chen, K.J. Gaskell, X. He, Y.J. Liang, J.J. Jiang, C.S. Wang, Solid-state electrolyte anchored with a carboxylated azo compound for all-solid-state lithium batteries, Angew. Chem. Int. Ed. 57 (2018) 8567–8571.

[2] J.C. Bachman, S. Muy, A. Grimaud, H.H. Chang, N. Pour, S.F. Lux, O. Paschos, F. Maglia, S. Lupart, P. Lamp, L. Giordano, Y. Shao-Horn, Inorganic solid-state electrolytes for lithium batteries: mechanisms and properties governing ion conduction, Chem. Rev. 116 (2015) 140–162.

[3] B. Zhang, T. Rui, L. Yang, J. Zheng, K. Zhang, S. Mo, L. Zhan, P. Feng, Mechanisms and properties of ion-transport in inorganic solid electrolytes, Energy Storage Mater 10 (2018) 139–159.

[4] Y. Kato, S. Hori, T. Saito, K. Suzuki, M. Hirayama, A. Mitsui, M. Yonemura, H. Iba, R. Kanno, High-power all-solid-state batteries using sulfide superionic conductors, Nat. Energy 1 (2016) 16030.

[5] Y. Wang, X. Lü, C. Zheng, X. Liu, Z. Chen, W. Yang, J. Lin, F. Huang, Chemistry design towards a stable sulfide-based superionic conductor $Li_4Cu_8Ge_3S_{12}$, Angew. Chem. Int. Ed. 58 (2019) 1–6.

[6] C. Yu, S. Ganapathy, E.R.H.V. Eck, H. Wang, S. Basak, Z. Li, M. Wagemaker, Accessing the bottleneck in all-solid state batteries, lithium-ion transport over the solid-electrolyte-electrode interface, Nat. Commun. 8 (2017) 1086.

[7] Z. Zhang, Y. Shao, B.V. Lotsch, Y.S. Hu, L. Chen, New horizons for inorganic solid state ion conductors, Energy Environ. Sci. 11 (2018) 1945–1976.

[8] S.S. Duan, H.Y. Jin, J.X. Yu, E.N. Esfahani, B. Yang, J.L. Liu, Y.Z. Ren, Y. Chen, L. H. Lu, X.C. Tian, S.E. Hou, J.Y. Li, Non-equilibrium microstructure of $Li_{1.4}Al_{0.4}Ti_{1.6}(PO_4)_3$ superionic conductor by spark plasma sintering for enhanced ionic conductivity, Nano Energy 51 (2018) 19–25.

[9] S.D. Lee, K.N. Jung, H. Kim, H.S. Shin, S.W. Song, M.S. Park, J.W. Lee, Composite electrolyte for all-solid-state lithium batteries: low-temperature fabrication and conductivity enhancement, Angew. Chem. Int. Ed. 10 (2017) 1–8.

[10] J. Fu, Fast Li^+ ion conduction in Li_2O-Al_2O_3-TiO_2-SiO_2-P_2O_5 glass-ceramics, J. Am. Ceram. Soc. 80 (1997) 1901–1903.

[11] P. Hartmann, T. Leichtweiss, M.R. Busche, M. Schneider, M. Reich, J. Sann, P. Adelhelm, J. Janek, Degradation of NASICON-type materials in contact with lithium metal: formation of mixed conducting interphases (MCI) on solid electrolytes, J. Phys. Chem. C 117 (2013) 21064–21074.

[12] X. Xu, Z. Wen, Z. Gu, X. Xu, Z. Lin, Lithium ion conductive glass ceramics in the system $Li_{1.4}Al_{0.4}(Ge_{1-x}Ti_x)_{1.6}(PO_4)_3$ (x=0-1.0), Solid State Ion. 171 (2004) 207–213.

[13] H.S. Jadhav, C. Min-Seung, R.S. Kalubarme, L. Jong-Sook, J. Kyu-Nam, S. Kyoung-Hee, P. Chan-Jin, Influence of B_2O_3 addition on the ionic conductivity of $Li_{1.5}Al_{0.5}Ge_{1.5}(PO_4)_3$ glass ceramics, J. Power Sources 241 (2013) 502–508.

[14] X. Xu, Z. Wen, X. Wu, X. Yang, Z. Gu, Lithium ion-conducting glass–ceramics of $Li_{1.5}Al_{0.5}Ge_{1.5}(PO_4)_3$–$xLi_2O$ (x=0.0–0.20) with good electrical and electrochemical properties, J. Am. Ceram. Soc. 90 (2010) 2802–2806.

[15] L. Jian, Interfacial engineering of solid electrolytes, Journal of Materiomics 1 (2015) 22–32.

[16] S. André, T. Ahmet, F. Harald, B. Hartmut, M. Sevi, R. Bernhard, Fast interfacial ionic conduction in nanostructured glass ceramics, Phys. Rev. Lett. 98 (2007) 225901.

[17] C.M. Chang, Y.I. Lee, S.H. Hong, H.M. Park, Spark plasma sintering of $LiTi_2(PO_4)_3$-based solid electrolytes, J. Am. Ceram. Soc. 88 (2005) 1803–1807.

[18] K. Waetzig, A. Rost, U. Langklotz, B. Matthey, J. Schilm, An explanation of the microcrack formation in $Li_{1.3}Al_{0.3}Ti_{1.7}(PO_4)_3$ ceramics, J. Eur. Ceram. Soc. 36 (2016) 1995–2001.

[19] B.V.R. Chowdari, G.V.S. Rao, G.Y.H. LEE, XPS and ionic conductivity studies on Li_2O-Al_2O_3-(TiO_2 or GeO_2)-P_2O_5 glass-ceramics, Solid State Ion. 36 (2000) 1067–1075.

[20] D. Sonigra, S. Soman, A.R. Kulkarni, Effect of heat treatment time on microstructure and electrical conductivity in LATP glass ceramics, AIP Conference Proceedings 1591 (2014) 753–755.

[21] K.C. Sobha, K.J. Rao, Ac conductivity and transport studies in phosphate glasses with NASICON-type chemistry, Solid State Ion. 81 (1995) 145–156.

[22] S. Breuer, D. Prutsch, Q. Ma, V. Epp, F. Preishuber-Pflügl, F. Tietz, M. Wilkening, Separating bulk from grain boundary Li ion conductivity in the sol–gel prepared solid electrolyte $Li_{1.5}Al_{0.5}Ti_{1.5}(PO_4)_3$, J. Mater. Chem. 3 (2015) 21343–21350.

[23] M. Cheng, C. Kai, C. Liang, C.W. Nan, R. Ishikawa, K. More, M. Chi, Atomic-scale origin of the large grain-boundary resistance in perovskite Li-Ion-Conducting solid electrolytes, Energy Environ. Sci. 7 (2014) 1638–1642.

[24] J. Luo, Stabilization of nanoscale quasi-liquid interfacial films in inorganic materials: a review and critical assessment, Crit. Rev. Solid State 32 (2007) 67–109.

[25] C. Li, G. Lin, J. Maier, Enhancement of the Li conductivity in LiF by introducing glass/crystal interfaces, Adv. Funct. Mater. 22 (2012) 1145–1149.

[26] D. Zielniok, C. Cramer, H. Eckert, Structure/property correlations in ion-conducting mixed-network former glasses: solid-state NMR studies of the system Na_2O–B_2O_3–P_2O_5, Chem. Mater. 19 (2007) 3162–3170.

[27] W. Ślubowska, K. Kwatek, C. Jastrzębski, J.L. Nowiński, Thermal, structural and electrical study of boron-incorporated LATP glasses and glass-ceramics, Solid State Ion. 335 (2019) 129–134.

[28] J.S. Thokchom, B. Kumar, The effects of crystallization parameters on the ionic conductivity of a lithium aluminum germanium phosphate glass–ceramic, J. Power Sources 195 (2010) 2870–2876.

[29] K. Arbi, S. Mandal, J.M. Rojo, J. Sanz, Dependence of ionic conductivity on composition of fast ionic conductors Li1+xTi2-xAlx(PO4)3 , $0 \leq x \leq 0.7$. A parallel NMR and electric impedance study, Chem. Mater. 14 (2002) 1091–1097.

[30] H. Chen, H. Tao, Q. Wu, X. Zhao, Crystallization kinetics of superionic conductive Al (B, La)- incorporated $LiTi_2(PO_4)_3$ glass-ceramics, J. Am. Ceram. Soc. 96 (2013) 801–805.

[31] D. Qiu, P. Guerry, I. Ahmed, D.M. Pickup, D. Carta, J.C. Knowles, M.E. Smith, R. J. Newport, A high-energy X-ray diffraction, ^{31}P and ^{11}B solid-state NMR study of the structure of aged sodium borophosphate glasses, Mater. Chem. Phys. 111 (2008) 455–462.

[32] M. Pérez-Estébanez, J. Isasi-Marín, C. Díaz-Guerra, A. Rivera-Calzada, C. León, J. Santamaría, Influence of chromium content on the optical and electrical properties of $Li_{1+x}Cr_xTi_{2-x}(PO_4)_3$, Solid State Ion. 241 (2013) 36–45.

[33] S. Krimi, A.E. Jazouli, L. Rabardel, M. Couzi, I. Mansouri, G.L. Flem, Glass formation in the Na_2O-TiO_2-P_2O_5 system, J. Solid State Chem. 102 (1993) 400–407.

[34] R.J. Enez, A.D. Campo, M.L. Calzada, J. Sanz, S.D. Kobylianska, S.O. Solopan, A. G. Belous, Lithium $La_{0.57}Li_{0.33}TiO_3$ perovskite and $Li_{1.3}Al_{0.3}Ti_{1.7}(PO_4)_3$ Li-NASICON supported thick films electrolytes prepared by tape casting method, J. Electrochem. Soc. 163 (2016) A1653–A1659.

[35] B.H. Rita, P.R. Jean-Pierre, Raman microspectrometry applied to the study of electrode materials for lithium batteries, Chem. Rev. 110 (2009) 1278–1319.

[36] P. Jiang, B. Huang, L. Wei, F. Yan, X. Huang, Y. Li, S. Xie, K. Pan, Y. Liu, J. Li, Resolving fine electromechanical structure of collagen fibrils via sequential excitation piezoresponse force microscopy, Nanotechnology 30 (2019) 205703.

[37] B. Huang, E.N. Esfahani, J. Li, Mapping intrinsic electromechanical responses at the nanoscale via sequential excitation scanning probe microscopy empowered by deep data, Natl. Sci. Rev. 6 (2018) 55–63.

[38] J. Li, J.F. Li, Y. Qi, N.C. Qian, S. Xie, Strain-based scanning probe microscopies for functional materials, biological structures, and electrochemical systems, Journal of Materiomics 1 (2015) 3–21.

[39] X. Shuhong, G. Anil, C.Q. Nataly, L. Yuanming, Z. Yichun, P. Roger, L. Jiangyu, High resolution quantitative piezoresponse force microscopy of $BiFeO_3$ nanofibers with dramatically enhanced sensitivity, Nanoscale 4 (2012) 408–413.

[40] N.C. Qian, Y. Liu, Y. Liu, S. Xie, G. Cao, J. Li, Delineating local electromigration for nanoscale probing of lithium ion intercalation and extraction by electrochemical strain microscopy, Appl. Phys. Lett. 101 (2012), 063901.

[41] N. Balke, S. Jesse, Y. Kim, L. Adamczyk, A. Tselev, I.N. Ivanov, N.J. Dudney, S. V. Kalinin, Real space mapping of Li-ion transport in amorphous Si anodes with nanometer resolution, Nano Lett. 10 (2010) 3420–3425.

[42] S.Y. Luchkin, K. Romanyuk, M. Ivanov, A.L. Kholkin, Li transport in fresh and aged $LiMn_2O_4$ cathodes via electrochemical strain microscopy, J. Appl. Phys. 118 (2015), 072016.

[43] S. Yang, B. Yan, J. Wu, L. Lu, K. Zeng, Temperature-dependent lithium-ion diffusion and activation energy of $Li_{1.2}Co_{0.13}Ni_{0.13}Mn_{0.54}O_2$ thin-film cathode at nanoscale by using electrochemical strain microscopy, Acs Appl. Mater. Inter. 9 (2017) 13999–14005.

[44] N.C. Qian, S.B. Adler, J. Li, Imaging space charge regions in Sm-doped ceria using electrochemical strain microscopy, Appl. Phys. Lett. 105 (2014) 183902.

[45] B.J. Rodriguez, C. Callahan, S.V. Kalinin, R. Proksch, Dual-frequency resonance-tracking atomic force microscopy, Nanotechnology 18 (2007) 475504.